Front. Energy 2024, 18(6): 863–874
https://doi.org/10.1007/s11708-024-0964-2

RESEARCH ARTICLE

Core-membrane microstructured amine-modified mesoporous biochar templated via $ZnCl_2$/KCl for CO_2 capture

Chen Zhang[1,2], Duoyong Zhang[1,2], Xinqi Zhang[2,3], Yongqiang Tian[4], Liwei Wang (✉)[1,2]

1 Institute of Refrigeration and Cryogenics, Key Laboratory of Power Machinery and Engineering (Ministry of Education), Shanghai Jiao Tong University, Shanghai 200240, China
2 Shanghai Non-carbon Energy Conversion and Utilization Institute, Shanghai 200240, China
3 China-UK Low Carbon College, Shanghai Jiao Tong University, Shanghai 201306, China
4 College of Smart Energy, Shanghai Jiao Tong University, Shanghai 200240, China

Abstract Mesoporous biochar (MC) derived from biomass is synthesized using a dual-salt template method involving $ZnCl_2$ and KCl, followed by impregnation with polyethyleneimine (PEI) of varying average molecular weights under vacuum conditions to construct a core-membrane structure for enhancing carbon capture performance. The resulting MC exhibits a highly intricate network of micropores and abundant mesopores, along with defects in graphitic structures, effectively facilitating robust PEI loading. Among the PEI-modified samples, PEI-600@MC demonstrates the highest CO_2 sorption capacity, achieving approximately 3.35 mmol/g at 0.1 MPa and 70 °C, with an amine efficiency of 0.32 mmol CO_2/mmol N. The introduction of amine functional groups in PEI significantly enhances the sorption capacity compared to bare MC. Additionally, PEI with lower average molecular weights exhibits a superior sorption performance at low pressures but shows a reduced thermal stability compared to higher molecular weight counterparts. The area of sorption hysteresis loops gradually decreases with increasing temperature and average molecular weight of PEI. The equilibrium sorption isotherms are accurately modeled by the Langmuir equation, revealing a maximum sorption capacity of approximately 3.53 mmol/g at 70 °C and saturation pressure. This work highlights the potential of dual-salts templated biomass-derived MC, modified with PEI, as an effective, widely available, and cost-efficient material for CO_2 capture.

Keywords mesoporous biochar (MC), dual-salt templated, carbon dioxide capture, sorption, polyethyleneimine (PEI)

1 Introduction

The realm of carbon dioxide (CO_2) capture technologies, essential for mitigating industrial emissions, has become a focal point of extensive inquiry in recent years [1–5]. Among the array of sorbents scrutinized, those endowed with nitrogen-containing functional groups have ascended as prime contenders, owing to their prodigious sorption capacity and discernible selectivity [6–11]. Noteworthy among these are several small molecules, such as ethylenediamine [12], tetraethylenepentamine [13], monoethanolamine [14], diethanolamine [15], and triethylenetetramine [16], which have exhibited a commendable efficacy in CO_2 trapping albeit marred by suboptimal robustness. Polyethyleneimine (PEI), lauded for its ubiquitous presence in research endeavors attributable to its remarkable CO_2 sorption capacity, expeditious sorption kinetics, commendable robustness, and economic viability [17,18].

The wet impregnation method, a stalwart technique, finds frequent application in the immobilization of PEI onto mesoporous substrates characterized by pore dimensions spanning 2–50 nm. In a notable exploration, biomass sawdust surfaced as an environmentally conscientious scaffold for PEI-600, demonstrating a commendable sorption capacity nearing 1.2 mmol/g at 0.1 MPa and 100 °C [19]. Nonetheless, the confined

Received Jul. 18, 2024; accepted Sept. 29, 2024; online Oct. 30, 2024
Correspondence: Liwei Wang, lwwang@sjtu.edu.cn

porosity of sawdust imposes limitations on PEI anchoring. To surmount this hurdle, alternative mesoporous matrices boasting superior microstructural attributes, such as layered double hydroxide [20], mesoporous silica [21], γ-Al_2O_3 [22], and mesoporous carbon [23], have been scrutinized for PEI deposition. Nanoarchitectures comprising self-assembled particles adorned with abundant slit-like mesopores, broad pore size distribution, and copious defects foster homogeneous dispersion of impregnated PEI, thereby facilitating optimal diffusive interplay with CO_2 molecules [20]. Moreover, Santa Barbara Amorphous-15 (SBA-15), characterized by a broader pore diameter ranging 6–11 nm and impregnated with 60 wt.% PEI (wt.% represents mass fraction), showcases a peak sorption capacity nearing 1.14 mmol/g at 400 mg/L CO_2 and 25 °C, eclipsing PEI supported by MCM-41 (pore diameter around 2–3.5 nm) and MCM-48 (pore diameter approximately 2.6 nm) under analogous conditions [21]. This revelation underscores the direct correlation between sorption performance and mesoporous dimensions. Consequently, PEI-loaded mesoporous carbon spheres exhibited a superlative sorption capacity approaching 3.22 mmol/g at 75 °C, attributable to their pristine spherical morphology, expansive specific surface area, and substantial pore volume [23]. The deployment of mesoporous carbon as a scaffolding substrate for PEI deposition in CO_2 capture endeavors holds immense promise, courtesy of its prodigious specific surface area and pore diameter [24,25].

The template method serves as the cornerstone for fabricating mesoporous carbon, categorized into either the hard template or the soft template method, contingent upon the nature of the template employed [26]. Traditionally, hard templates, predominantly comprising mesoporous silicon [27] and minerals [28], are harnessed, yielding mesoporous carbon architectures that mirror the inverse structure of the templates [29]. Nonetheless, the hard template methodology is entwined with elevated costs and intricate preparation protocols owing to the requisite template removal via solvent dissolution, a process fraught with recycling challenges [30]. In stark contrast, the soft template method leverages economically viable triblock copolymers, notably F127, F108, F68, and P123, to engender mesopores of diminished dimensions vis-à-vis the hard template approach, thus constraining the impregnation capacity of PEI [31]. Encouragingly, the adoption of alkali metal chlorides, particularly KCl [32] and $ZnCl_2$ [33], as templates for the biomass-derived mesoporous biochar (MC), endowed with microstructures featuring larger pore dimensions, has garnered attention. The incorporation of KCl in the salt template methodology promotes defect formation, providing anchorage sites for PEI [32]. Additionally, KCl acts as an activating agent for biomass [34,35], resulting in the development of abundant microporous structures with yields exceeding 80%. However, these micropores may become easily blocked by the PEI molecules during the impregnation process. Thus, $ZnCl_2$ facilitates mesopore generation via inducing the collapse of the carbonaceous framework of biomass, albeit at the expense of diminished carbon yield [33]. The salt template approach proffers manifold benefits, including a streamlined, eco-friendly, and cost-efficient fabrication trajectory, bolstered by the recyclability and reusability of alkali metal chlorides [36].

To date, considerable researches have focused on developing MC with defective structures. However, a notable gap remains in the study of salt-templated MC featuring larger pore dimensions. In this investigation, this paper introduces a novel preparatory method that involves the carbonization of biomass, employing dual-salt templates, $ZnCl_2$ and KCl. This process is followed by wet impregnation under vacuum conditions to create a foundational scaffold for PEI integration, resulting in a core-membrane microstructured amine-modified MC. The resultant materials undergo comprehensive characterization, including surface properties, porous morphology, thermal stability, phase composition, and functional groups. Subsequent to the characterization, it systematically examines and evaluates the sorption performance of the core-membrane microstructured amine-modified MC.

2 Materials and methods

2.1 Materials

The waste corncob utilized in this investigation originates from Xinjiang Uygur Autonomous Region and serves as the biochar precursor. Methanol (MeOH, analytical grade, ⩾ 99.5%), zinc chloride ($ZnCl_2$, 99%), and potassium chloride (KCl, ⩾ 99.6%) are procured from Sinopharm Chemical Reagent, 3A, and Adamas-Life, respectively. Three variants of PEI exhibiting distinct average molecular weights of 600, 1800, and 10000 are supplied by Aladdin. Helium, CO_2, and N_2 gases are sourced from Liquefied Air (Shanghai) Compressed Gas. All chemicals are employed as received, obviating the necessity for supplementary purification measures.

2.2 Fabrication of materials

The preparation of MC adheres to the modified dual-salt template method, as originally delineated by Ma et al. [37]. In this investigation, corncob powder (100 mesh) serves as a substitute for glucose, microcrystalline cellulose, and lignin as the biochar precursor. Typically, 21.9 wt.% of KCl and 38.2 wt.% of $ZnCl_2$ are dissolved in deionized water to fabricate the dual-slat template solution, with an additional 39.9 wt.% of corncob powder

introduced into the solution. Subsequently, the resultant suspension undergoes vigorously stirring for 1.5 h, followed by drying in an oven at 120 °C for 4 h to ensure thorough desiccation of the mixture. The desiccated mixture is then subjected to carbonization at a N_2 atmosphere utilizing a tubular furnace equipped with a gradient temperature program. The temperature ascends from ambient to 240 °C at a heating rate of 3 °C/min, where it is maintained for 2 h. Subsequently, the temperature is incrementally elevated to 1000 °C at a heating rate of 1 °C/min, and held steady at 1000 °C for 2 h. Upon cooling to room temperature at the N_2 atmosphere, the mixture undergoes washing with excess deionized water at room temperature to eradicate the templates. The resulting sample is subsequently filtered with a 200-mesh sieve and dried under vacuum at 120 °C overnight.

The preparation of core-membrane microstructured PEI-modified MC (PEI@MC) entails the wet impregnation technique under vacuum conditions. Initially, a predetermined quantity of PEI with varying average molecular weights is dispersed in methanol. Subsequently, the MC powders are introduced into the PEI methanol solution. The impregnation process transpires under vacuum for a duration of 4 h. Following impregnation, the mixture undergoes rotary evaporation at 60 °C and 40 r/min under vacuum conditions until complete volatilization of the methanol solvent. The resultant products are subsequently dried at 60 °C under vacuum overnight to ensure the complete removal of methanol solvent. These products are designated as PEI-*X*@MC, where '*X*' denotes the average molecular weights of PEI, with values of 600, 1800, and 10000.

2.3 Characterization

The microcosmic morphologies and elemental mapping of MC and PEI@MC sorbents are examined via scanning electron microscopy (SEM) equipped with energy dispersive spectrometer (EDS) functionality, utilizing a Regulus 8100 microscope manufactured by Japan Hitachi. Additionally, pore morphologies are elucidated using transmission electron microscopy (TEM) with a Tecnai G2 F20 instrument by FEI America. Nitrogen adsorption/desorption isotherms are recorded at 77 K employing a TriStar II 3020 instrument by Micromeritics America. The specific surface area (S_{BET}) is derived via the Brunnauer-Emmett-Teller (BET) method, based on the isothermal data obtained within a relative pressure range from 0.005 to 0.1. Micropore volume (V_0) and total pore volume (V_t) are determined utilizing the t-plot method and measuring N_2 sorption capacity at a relative pressure of 0.99, respectively. The average pore diameter (d_a) is calculated from the total pore volume and BET surface area. Furthermore, the particle size of the samples is analyzed using a Zetasizer Nano ZS90 (Malvern England) to assess the size distribution and ensure consistency in the sample morphology. Thermal robustness of both the MC and PEI@MC sorbents is evaluated via thermogravimetry coupled with differential scanning calorimetry (TG-DSC) on a TGA/DSC 3+ instrument by Mettler Toledo in Switzerland. Moreover, surface properties of the samples are assessed by Fourier-transform infrared spectroscopy (FT-IR) utilizing a Nicolet iS50 FT-IR spectrometer by Thermo American. Crystallinity is analyzed through X-ray diffraction (XRD) and Raman spectra conducted in a SmartLab (3 kW) instrument by Rigaku Japan and a LabRAM HR Evolution system by HORIBA France (λ = 532 nm), respectively. Surface elemental composition is determined employing X-ray photoelectron spectroscopy (XPS) with an ESCELAB 250XI instrument by Thermo America. Bulk elemental analysis of carbon (C), hydrogen (H), oxygen (O), and nitrogen (N) is conducted using a Vario EL cube instrument produced by Elementar in Germany.

2.4 CO_2 sorption experiments

The equilibrium sorption isotherms of the samples are determined utilizing a high- and low-pressure adsorption analyzer (H-Sorb 2600TL, Ultmetrics China) to meet the requirement of fixed-bed condition, with measurements conducted across a temperature range of 50 to 110 °C and a pressure span from 0.005 to 0.1 MPa. Following sorption, desorption is performed under vacuum at the same sorption temperature. Prior to sorption measurements, the samples are pretreated at 100 °C for 3 h with a heating rate of 8 °C/min to ensure complete desorption of any previously sorbed gas, typically H_2O. These experimental equilibrium sorption isotherms provide valuable insights into the sorption parameters such as the sorption capacity, sorption hysteresis, and amine efficiency, thus elucidating a detailed evaluation on sorption behavior and performance of the materials under the tested conditions.

Additionally, the sorption cyclic robustness is assessed by performing 20 cycles of vacuum pressure swing sorption and vacuum temperature swing sorption with the same equipment under identical pretreatment conditions. Sorption selectivity ($S_{C/N}$) is calculated from the experimental sorption isotherms using the ideal adsorption solution theory (Eq. (1)), which quantifies the relative affinity of the sorbent for CO_2 over N_2, reflecting their capacity to preferentially capture CO_2 from a gas mixture.

$$S_{C/N} = \frac{x_{CO_2}/x_{N_2}}{y_{CO_2}/y_{N_2}}, \tag{1}$$

where x_{CO_2} and x_{N_2} represent the molar fractions of CO_2 and N_2 in the samples, respectively, while y_{CO_2} and y_{N_2} denote the molar fractions of CO_2 and N_2 in the feed gas,

individually.

Furthermore, various isothermal models, including the Langmuir model (Eq. (2)), Freundlich model (Eq. (3)), Toth model (Eq. (4)), Sips model (Eq. (5)), and Temkin model (Eq. (6)), are employed to reconstruct and analyze the experimental equilibrium sorption isotherm data. By fitting the experimental sorption data to these isothermal models, the parameters of each model are determined, facilitating a comprehensive comprehension on the sorption behavior of the samples. Additionally, comparison between different models allows for the evaluation of their suitability in describing the experimental data.

$$q = q_{\mathrm{m}} \frac{Bp}{1 + Bp}, \tag{2}$$

$$q = Kp^{1/n}, \tag{3}$$

$$q - q_{\mathrm{m}} \frac{Bp}{\left[1 + (Bp)^n\right]^{1/n}}, \tag{4}$$

$$q = q_{\mathrm{m}} \frac{Bp^n}{1 + Bp^n}, \tag{5}$$

$$q = B\ln(Ap), \tag{6}$$

where p and q represent pressure and sorption capacity, separately, while A, B, K, and n are fit parameters.

3 Results and discussion

3.1 Microcosmic morphology

The microcosmic morphology analysis depicted in Fig. 1 unveils the distinctive porous structure characteristic of biomass-derived MC and core-membrane microstructured PEI-modified MC. SEM imaging of the surface of MC (Fig. 1(a)) showcases an abundance of randomly distributed pores, contributing to a highly porous microstructure with a substantial surface area. The presence of $ZnCl_2$ within the dual-salt template is instrumental in introducing the collapse of localized carbon frameworks within the biomass, thereby augmenting the development of the porous microstructure. However, in the context of core-membrane microstructured PEI-modified MC, exemplified by PEI-600@MC, the SEM image (Fig. 1(b)) illustrates the formation of a substantial viscous PEI membrane atop the MC surface, overcoming liquid surface tension, with the bulk of PEI loaded within the MC pores. This membrane partially obstructs certain pores, constraining N_2 molecule access to these specific regions via diffusion as the gaseous molecules. Nevertheless, CO_2 molecules are facilitated in selectively diffusing within the membrane and the PEI-laden pores through liquid-phase mass transfer processes, optimizing the utilization of amine functional groups in PEI, which react chemically with CO_2 [38]. Moreover, EDS analysis (Fig. 1(c)) demonstrates a pronounced increase in N and O elements on the surface of PEI-600@MC compared to bare MC, affirming the successful formation of a PEI membrane enriched with amine and hydroxyl functional groups. Additionally, the TEM images of MC and PEI-600@MC (Figs. 1(d) and 1(e)) reveal the presence of well-defined worm-like mesoporous structures and demonstrate the pore-filling effect due to the incorporation of PEI molecules. Specifically, the refined TEM image in Fig. 1(e) highlights the formation of a distinct PEI membrane microstructure, with an observed thickness of approximately 5.4 nm.

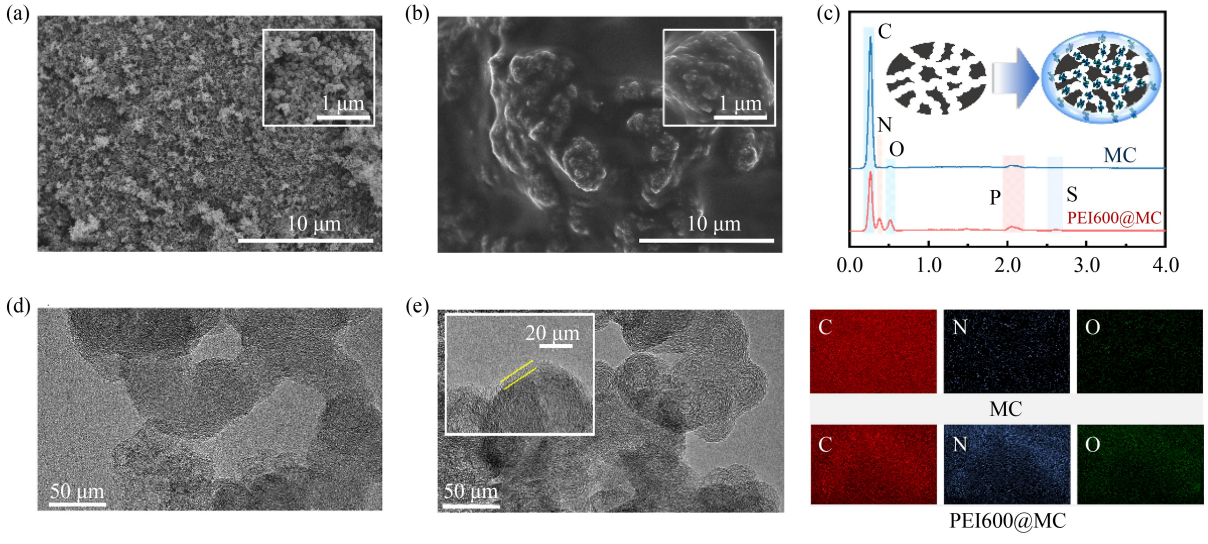

Fig. 1 Microcosmic morphology of biomass-derived MC and core-membrane microstructured PEI-modified MC.
(a) SEM images of MC; (b) SEM images of PEI-600@MC; (c) EDS analysis; (d)TEM images of MC; (e) TEM images of PEI-600@MC.

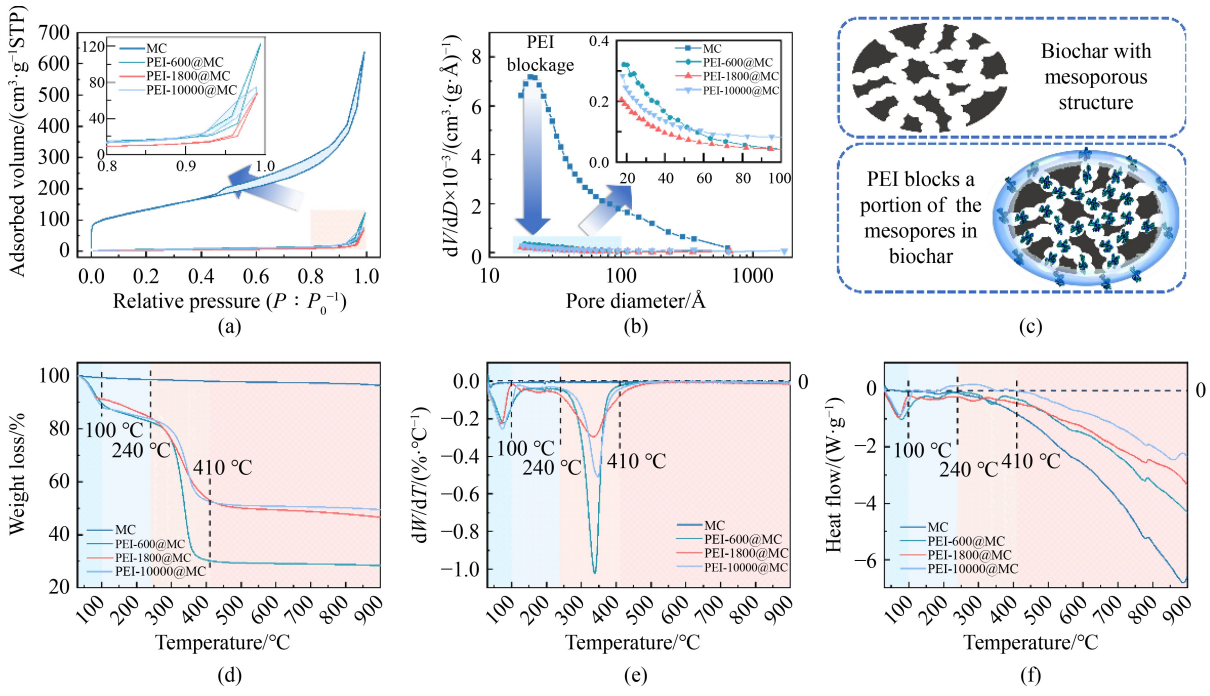

Fig. 2 Porous properties and thermal robustness of biomass-derived MC and core-membrane microstructured PEI-modified MC. (a) N_2 adsorption–desorption isotherms; (b) pore size distributions; (c) core-membrane microstructures; (d) TGA; (e) DTG; (f) DSC.

3.2 Porous properties and thermal robustness

The porous properties of biomass-derived MC and core-membrane microstructured PEI-modified MC are scrutinized through N_2 adsorption–desorption isotherms at 77 K (Fig. 2(a)) to facilitate deeper insights. MC demonstrates a type IV isotherm per the IUPAC (International Union of Pure and Applied Chemistry) classification, indicative of highly developed microporosity, evidenced by substantial N_2 adsorption at a low relative pressure ($P/P_0 < 0.01$). The presence of a hysteresis loop at higher relative pressures ($P/P_0 > 0.4$) suggests the existence of significant mesopores within the MC sorbent. Conversely, PEI@MC sorbents exhibit type III isotherms (Fig. 2(a)), signifying a diminished presence of mesopores and micropores due to the obstruction of massive microporous within the MC framework by the surface PEI membrane, alongside the anchoring of extensive mesoporous regions by PEI molecules. In addition, the lower adsorption capacities of PEI@MC sorbents at a low relative pressure stem from weaker interactions between residual mesopores in the sorbents and N_2 molecules compared to the interactions within micropores of MC or between N_2 molecules themselves. Furthermore, pore size distribution analysis of MC (Fig. 2(b)) unveils the presence of mesopores ranging from 20 to 500 Å. These mesopores serve as anchoring sites for PEI, facilitating the extension of PEI molecules from the mesopores to the surface of biochar through the combined effect of liquid surface tension and the viscosity of PEI. This phenomenon further leads to the formation of core-membrane microstructures (Fig. 2(c)). Thus, in Fig. 2(b), the significant reduction observed in mesopore abundance post-modification with PEI underscores the pore blockage caused by the successful integration of PEI into the core-membrane microstructures of the sorbents.

Table 1 summarizes the detailed porous characteristics of biomass-derived MC and core-membrane microstructured PEI-modified MC. The MC exhibits a BET specific surface area of approximately 466 m^2/g, along with an average pore diameter of approximately 8.49 nm, which

Table 1 Detailed porous properties of biomass-derived MC and core-membrane microstructured PEI-modified MC

Samples	S_{BET}/($m^2 \cdot g^{-1}$)	V_t/($cm^3 \cdot g^{-1}$)	V_0/($cm^3 \cdot g^{-1}$)	V_m/($cm^3 \cdot g^{-1}$)	d_a/nm	Density/($g \cdot cm^{-3}$)
MC	465.74	0.9880	0.0146	0.9734	8.49	0.5394
PEI-600@MC	22.64	0.1912	0.0000	0.1912	33.78	0.8672
PEI-1800@MC	13.87	0.1052	0.0000	0.1052	30.33	0.8707
PEI-10000@MC	19.41	0.1167	0.0000	0.1167	24.06	0.8597

Notes: S_{BET} represents the specific surface area calculated by BET method; V_t, V_0, and V_m represent total pore volume, micropore volume, and mesopore volume, respectively; d_a is the average pore diameter.

is lower than that of the other biochar prepared by glucose [37]. The mesopore volume ratio (V_m/V_t) of MC is notably high at 98.52%, providing adequate mesopore volume for PEI anchoring and promoting the extension of the PEI membrane. Conversely, PEI@MC sorbents display fluctuating BET specific surface areas ranging from 13.98 to 22.63 m^2/g, indicating a decrease compared to bare MC. Total pore volume (V_t) and mesopore pore volume (V_m) vary from 0.1052 to 0.1912 cm^3/g, suggesting an attenuation in porosity after PEI loading. Additionally, the average pore diameter decreases with increasing average molecular weights of PEI, highlighting the impact of PEI loading as membrane on the porous microstructure of the sorbents. All samples exhibit a single prominent particle size distribution peak between 100 nm and 200 nm (Fig. S1). Moreover, the densities of core-membrane microstructured PEI-modified MC are approximately 60% higher than those of biomass-derived MC (Table S1 and Table 1). Overall, MC possesses a highly developed mesopore microstructure with a large mesopore ratio and adequate mesopore volume, while PEI@MC sorbents exhibit a decreased surface area and an attenuated porosity due to PEI membrane. Notably, after sorbing CO_2, the detailed porous properties of PEI-600@MC do not undergo significant changes, apart from a reduction in pore volume, attributed to the sorbed CO_2 (Table S2 and Fig. S2).

The thermal robustness of biomass-derived MC and core-membrane microstructured PEI-modified MC is meticulously assessed through TGA-DSC with derivative thermo-gravimetry (DTG), unraveling intricate weight loss behaviors across a broad temperature, in the temperature spectrum of 30–900 °C, as delineated in Figs. 2(d)–2(f). Below 100 °C, all PEI@MC variants exhibit a subtle endothermic peak (Fig. 2(f)), attributed to the desorption of encapsulated gas molecules. In stark contrast, the derivative weight loss (Fig. 2(e)) and heat flow (Fig. 2(f)) of MC within this temperature regime remain negligible owing to the limited number of micropores capable of directly entrapping gas molecules from the atmosphere. However, PEI@MC sorbents display a discernible weight loss of up to 10% in this temperature range (Fig. 2(d)), primarily attributable to spontaneous sorption and subsequent reaction of steam and CO_2 in the ambient air facilitated by the amine functional groups in PEI. Particularly noteworthy is the rapid mass reduction observed exclusively among the PEI@MC sorbents within the temperature band of 240–400 °C (Fig. 2(d)), with distinct chemical processes discernible contingent upon the average molecular weights of PEI. In instances where PEI with smaller average molecular weights (600 and 1800) is employed, a modest endothermic peak is apparent (Fig. 2(f)), indicating the escape of PEI from the sorbents as elevated temperatures furnish adequate energy to surmount anchoring interactions and membrane structure constraints. Conversely, PEI-10000@MC manifests a broad exothermic peak (Fig. 2(f)), signifying the oxidation reaction of PEI-10000. The intensified interactions between PEI with large average molecular weights and a greater abundance of hydrogen bonds vis-à-vis MC impede the escape of PEI. Furthermore, the temperature at which the peak of DTG occurs progressively escalates with the enhancement of average molecular weight (Fig. 2(e)), underscoring the favorable impact of high molecular weight on bolstering thermal robustness. Notably, both the biochar skeleton of PEI@MC sorbents and the MC undergo the release of residual volatile substances alongside the oxidation of the biomass carbon skeleton above 410 °C, accompanied by marginal weight loss (Fig. 2(d)). Collectively, PEI@MC sorbents evince remarkable thermal robustness below 240 °C, surpassing the typical capturing temperature of conventional amine-modified CO_2 capture materials. This underscores the capacity of PEI@MC sorbents to endure the requisite operating conditions for CO_2 capture applications sans significant deactivation.

3.3 Phase structure

Figure 3(a) presents the XRD profiles of both biomass-derived MC and core-membrane microstructured PEI-modified MC. Two distinct diffraction peaks at 23.5° and 43° are consistently observed across all samples, ascribing to the (002) and (100) planes of graphene, respectively [39]. The presence of these peaks strongly suggests the formation of graphitic structures within the MC matrices. Furthermore, the amorphous characteristics of the samples are probed via Raman spectroscopy, as illustrated in Fig. 3(b). Here, two prominent signals emerge at approximately 1350 and 1580 cm^{-1}, corresponding to the defect bands (D-band) and graphitic bands (G-band), respectively [40]. The D-band arises from the A_{1g} mode of defective carbons, pivotal in creating microstructures and microenvironments conducive to PEI anchoring and robust core-membrane formation. Conversely, the G-band corresponds to the E_{2g} mode for sp^2-hybridized graphitic carbons, augmenting heat conductivity. Hence, the I_D/I_G ratios of MC and PEI-modified MC exceed 1.14 with more D-band, contributing to constructing the core-membrane structure of CO_2 capture. These distinctive signals in the Raman spectra offer crucial insights into the structural properties of the samples, underscoring the significance of defect-rich graphitic structures as pivotal sites for modification.

Figure 3(c) elucidates the molecular structure of branched PEI and further dissects the unique functional groups introduced into MC through PEI loading. Both XRD and Raman spectra confirm composition of MC as graphene, while PEI molecules exhibit primary amines, secondary amines, tertiary amine, C−H_2 bonds, and N−H bonds. Moreover, FT-IR analysis (Fig. 3(d)) sheds light

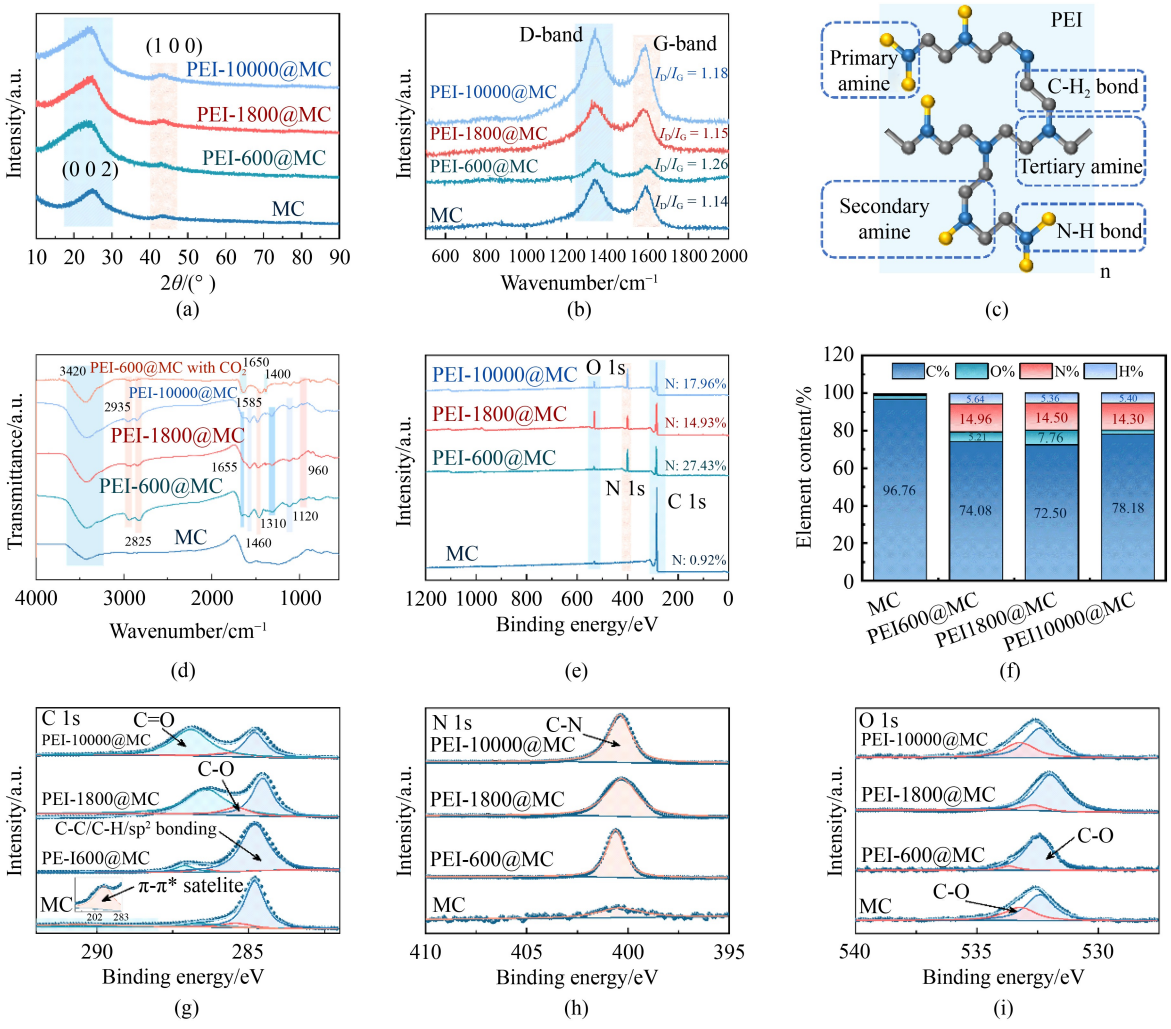

Fig. 3 Phase structure characterization profiles of biomass-derived MC and core-membrane microstructured PEI-modified MC. (a) XRD; (b) Raman; (c) structure of branched PEI; (d) FT-IR; (e) XPS spectra for survey scans; (f) bulk elemental analysis; (g) C 1s; (h) N 1s; (i) O 1s.

on the surface functionalities of both biomass-derived MC and core-membrane microstructured PEI-modified MC. In the spectrum of MC, a broad band centered around 3420 cm^{-1} is typically attributed to the stretching vibration of surface hydroxylic groups [41]. Post-impregnation with PEI, a reduction in transmittance in this peak is observed, attributed to the stretching vibration of N−H in PEI molecules. Notably, several novel peaks emerge in the FT-IR spectra of PEI@MC sorbents, including bands at 2935 and 2825 cm^{-1}, corresponding to the asymmetric and symmetric stretching of C-H_2 in the carbon chain of PEI, respectively [42]. Additionally, the band at 1460 cm^{-1} is ascribed to the bending vibration of C−H_2 [43]. Peaks at 1655 and 1585 cm^{-1} are primarily associated with the asymmetric and symmetric bending vibrations of the primary amine (−NH_2) and secondary amine (−N(R)H), respectively [43], with their stretching vibrations manifested 1310 and 1120 cm^{-1}. Moreover, a small peak occurring at 960 cm^{-1}, beyond the range of their stretching vibration, suggests the presence of tertiary amine (−$N(R)_2$) structures in the branched PEI. Collectively, the emergence of new peaks corresponding to functional groups in PEI by FT-IR analysis confirms the successful loading of PEI onto the surface of MC. Furthermore, new characteristic peaks appear at 1650 and 1400 cm^{-1} in the PEI-600@MC after CO_2 sorption, corresponding to the C=O and C−N bonds in the −CONH− groups generated during the sorption process, respectively. These peaks confirm that the CO_2 sorption mechanism of core-membrane microstructured PEI-modified MC is based on a chemical reaction.

XPS analysis offers further insights into the chemical structures and syntactic arrangement of both biomass-derived MC and core-membrane microstructured PEI-modified MC. Survey scans (Fig. 3(e)) affirm the presence of C, N, and O elements on the surface of samples, indicative of the substantial enrichment of N

element. Particularly, the surface nitrogen content of PEI-600@MC is measured at 27.43%, whereas that of MC stands around 0.92%. However, bulk phase element analysis (Fig. 3(f)) highlights that PEI-600@MC sorbent possesses approximately 14.96% N, constituting only 54.5% of the nitrogen content on its surface, the lowest among all the PEI@MC sorbents. This observation suggests a relatively higher concentration of surface N in PEI-600@MC compared to its bulk nitrogen content, indicating a greater abundance of amine functional groups attached to the surface membrane structure, potentially enhancing its performance in CO_2 capture applications. The fitted curves and Gaussian deconvoluted peaks of C 1s, N 1s, and O 1s spectra are depicted in Figs. 3(g)–3(i). The band observed at approximately 284.8 eV in Fig. 3(g) is attributed to the C−C [44], C−H [45], and sp^2 bonding [46] in the biomass-derived MC. Additionally, the presence of a π-π* satellite at 290.6 eV [47] serves as a further evidence of graphene formation [48] as corroborated by XRD and Raman spectra. Upon building the PEI membrane on the surface of biomass-derived MC, unique C−N functional groups of newly introduced PEI molecules appear at 400.4 eV [49] (Fig. 3(h)). Furthermore, newly formed peaks at 285.4 eV (C−O [50]) and 286.6 eV (C=O [50]) confirm the existence of partially oxidized clusters in PEI molecules, supported by bonds at 532.4 eV (C=O [51]) and 533.2 eV (C−O [52]) in the O 1s spectra (Fig. 3(i)). The integral area of oxidized functional groups increases with rising average molecular weight, indicative of sorption sites being occupied to reduce sorption reaction activity.

3.4 Sorption properties

Figure 4 and Table 2 illustrate the sorption performance of both biomass-derived MC and core-membrane microstructured PEI-modified MC, revealing an augmentation in sorption capacity with increasing pressure. Initially, MC demonstrates a modest sorption capacity of only 0.19 mmol/g CO_2 (0.11 g/mL) at 50 °C and 0.1 MPa, with no noticeable sorption hysteresis (Fig. 4(a)), indicative of a predominantly physisorption-based process. Its sorption isothermal is classified as type III or type V isotherms, suggesting the presence of a well-developed mesoporous structure but a lack of strong chemisorption sites or sufficient micropores necessary for efficient CO_2 capture. However, the introduction of PEI dramatically enhances the sorption capacities of MC between 50 to 110 °C, due to the integration of amine functional groups within the core-membrane microstructure (Fig. 4(b)). These amine functional groups chemically react with CO_2 to form ammonium carbamates at relatively low pressures, following the reaction pathway outlined in Eq. (7) [38,53], as confirmed by FT-IR analysis.

$$2RNH_2 + CO_2 \rightleftarrows (RNH_2)^+ (COO)^- + RNH_2 \rightleftarrows (RNH_3)^+ (RNNHCOO)^- \quad (7)$$

The maximum sorption capacities are observed at 70 °C, which is the optimal reaction temperature for the chemisorption of CO_2 by amine functional groups. PEI-600@MC, PEI-1800@MC, and PEI-10000@MC achieve sorption capacities of approximately 3.35 mmol/g (2.91 mmol/mL), 2.79 mmol/g (2.43 mmol/mL), and 2.77 mmol/g (2.38 mmol/mL), respectively (Figs. 4(c)–(e)). The comparison of sorption capacities among the samples versus previously reported amine-modified mesoporous materials is summarized and tabulated in Table 2. Notably, the PEI-600@MC demonstrates a superior CO_2 sorption performance, especially at temperatures around 70 –75 °C, outperforming many previously reported PEI-modified mesoporous materials, as detailed in Table 2. Besides, the sorption isotherms of all PEI@MC sorbents at 50–90 °C resemble type I isotherms, while those at 110 °C exhibit type V behavior. The disparity between these two isotherm types lies in the sorption capacities at extremely low pressures, attributed to the temperature-sensitive sorption activity of amine functional groups gradually diminishing with raising temperature. Additionally, a comparation of sorption performance on MC modified by PEI membrane with various average molecular weights at the same temperature is conducted. The maximum sorption capacities at 50 °C exhibit similar trends to those at 70 °C, attenuating with increasing average molecular weights of PEI, albeit significantly lower at 50 °C. However, the maximum sorption capacities of PEI@MC sorbents at 90 and 110 °C display opposite trends compared to the those at lower temperatures, owing to the poor thermal robustness of low-average molecular weights PEI. Furthermore, the areas of sorption hysteresis loops, highlighted in Figs. 4(c)–4(e), are determined through integral calcula tion. The largest area is observed in PEI-600@MC sorbing at 50 °C due to stronger hysteresis effects, diminishing simultaneously with increasing temperature and average molecular weight of PEI.

Figure 4(f) summarizes the amine efficiency of core-membrane microstructured PEI-modified MC, with similar bulk nitrogen content among all PEI@MC sorbents. PEI-600@MC exhibits the highest amine efficiency among the sorbents, achieving a maximum value of approximately 0.32 mmol CO_2/mmol N at 70 °C. However, the amine efficiency of PEI-600@MC attenuates more rapidly than that of PEI-1800@MC and PEI-10000@MC. This underscores the optimal reaction temperature for PEI is around 70 °C. Excessive temperatures lead to a sharp decrease in amine efficiency, corresponding to the attenuation phenomenon of sorption capacity at high temperatures, while excessively low temperatures may not fully exploit the amine functional groups in PEI molecules due to limitations in diffusive interactions and

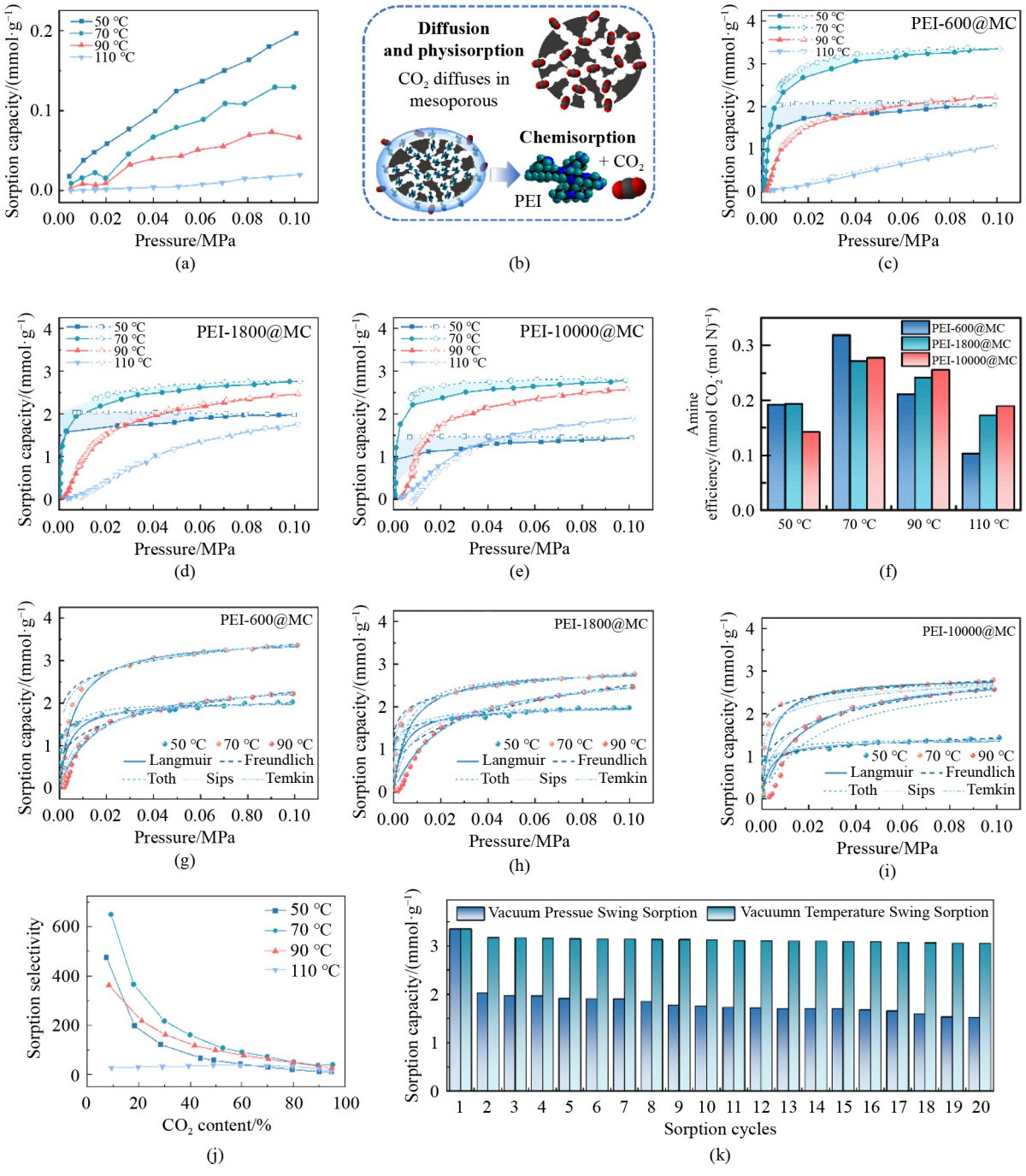

Fig. 4 Sorption performance of biomass-derived MC and core-membrane microstructured PEI-modified MC.

(a) MC; (b) sorption mechanism; (c) PEI-600@MC; (d) PEI-1800@MC; (e) PEI-10000@MC; (f) amine efficiency; (g) reconstructed isothermal of PEI-600@MC; (h) reconstructed isothermal of PEI-1800@MC; (i) reconstructed isothermal of PEI-10000@MC; (j) sorption selectivity of PEI-600@MC; (k) cyclic robustness of PEI-600@MC under vacuum pressure swing sorption. Notes: Solid and hollow symbols represent sorption and desorption, respectively.

reaction rate.

Figures 4(g)–4(i) depict the fitting results for the reconstructed equilibrium isotherms of the core-membrane microstructured PEI-modified MC using various isothermal models, including the Langmuir, Freundlich, Toth, Sips, and Temkin models, with acceptable regression correlation coefficients. It is noted that the Temkin model performs inadequately in accurately reconstructing the equilibrium sorption isotherms of samples, particularly at the low pressure, as evident in Figs. 4(g)–4(i). Conversely, the Freundlich model consistently yields fitting parameters (n) above 3.99, indicating a rapid increase in sorption capacity at relatively low pressures due to chemisorption sites. The Toth models and Sips models,

Table 2 Comparison of sorption capacity between core-membrane microstructured PEI-modified MC and previously reported PEI-modified mesoporous materials

PEI-modified mesoporous materials	Sorption capacity/ (mmol·g^{-1})	Temperature/ °C	Pressure/ MPa	Ref.
MC	0.13	70	0.1	This work
PEI-10000@MC	2.77	70	0.1	This work
PEI-1800@MC	2.79	70	0.1	This work
PEI-600@MC	3.35	70	0.1	This work
PEI-600@MC	2.68	70	0.015	This work
MC2-800–1-50 (PEI)	2.38	75	0.015	Sani et al. [54]
meso-AC-PEI600	1.30	75	0.01	Gibson et al. [55]
PEI-STPR-3	1.09	75	0.03	Tang et al. [56]
45PEI/MCNs	1.97	75	0.1	Chai et al.[57]
B-SiO_2-35PEI	1.48	70	0.015	Yan et al. [58]
PEI@AOMC	1.84	75	0.015	Kong et al. [59]

derived from Langmuir models with additional parameters, provide a more accurate forecast of the isotherms by considering the surface heterogeneity of core-membrane microstructure, albeit with greater model complexity. Among these models, the Langmuir model demonstrates excellent fitting performance with a regression correlation coefficient of 0.9990, highlighting its accuracy and simplicity in analyzing and interpreting sorption behaviors. Detailly, the Langmuir model predicts a maximum sorption capacity (q_m) for PEI-600@MC of 3.53 mmol/g at 70 °C, which is approximately 71.4% and 39.0% higher than the values at 50 and 90 °C, respectively (Table S3).

Figure 4(j) illustrates the sorption selectivity for the optimized core-membrane microstructured PEI-modified MC, specifically PEI-600@MC of CO_2 in a gas mixture balanced with N_2 at 0.1 MPa, using the ideal adsorption solution theory. The N_2 sorption capacity in the sorption isotherms remains below 0.04 mmol/g across 50 to 110 °C (Fig. S3). Within the temperature range of 50–90 °C, the sorption selectivity gradually decreases with the CO_2 concentration increasing with a peak reaching 649.8 at 70 °C due to the high amine efficiency at a low pressure. However, at 110°C, the chemisorption process weakens, resulting in a significant decline in selectivity, which fluctuates between 15 and 40 with varying CO_2 concentrations.

The cyclic robustness of PEI-600@MC is evaluated through vacuum pressure swing sorption (desorbing at 70 °C under vacuum) and vacuum temperature swing sorption (desorbing at 70 °C under vacuum). The initial CO_2 sorption capacity of PEI-600@MC is approximately 3.35 mmol/g, but it drops to 2.03 mmol/g in the second cycle of vacuum pressure swing sorption, with an attenuation exceeding 39.5% (Fig. 4(k)). However, under vacuum temperature swing sorption, PEI-600@MC demonstrates a remarkable recyclability, maintaining a stable sorption capacity of approximately 3.11 mmol/g over subsequent cycles with an average attenuation amplitude of less than 7.2%.

4 Conclusions

This paper has effectively showcased the utility of biomass-derived MC, templated by dual salts ($ZnCl_2$ and KCl), for proficient CO_2 capture. Through impregnation with PEI, it engineers core-membrane microstructured amine-modified MC. The biomass-derived MC reveals extensive mesopore structures with defect in graphitic structures, serving as anchoring sites for PEI. This facilitates the extension of PEI molecules from the mesopores to the biochar surface, aided by the combined effects of liquid surface tension and the PEI viscosity. The establishment of the core-membrane microstructure is substantiated by a comprehensive suite of characterization techniques employed.

Among the core-membrane microstructured PEI-modified MC samples, PEI-600@MC stands out with the highest CO_2 sorption capacities, reaching approximately 3.35 mmol/g at 70 °C and 0.1 MPa, alongside an amine efficiency of 0.32 mmol CO_2/mmol N. This marks a substantial enhancement over the biomass-derived MC, underscoring the pivotal role of amine functional groups in augmenting the sorption capacities. Moreover, it is observed that PEI-600, characterized by fewer oxidation deactivation functional groups, exhibits larger sorption capacities at extremely low pressures, albeit featuring poorer thermal robustness compared to PEI-1800 and PEI-10000. Additionally, the size of sorption hysteresis loops diminishes as both temperature and average molecular weight of PEI increase. The equilibrium sorption isotherms of the PEI@MC sorbents are effectively and accurately described by the Langmuir model, which reveals a maximum sorption capacity of approximately 3.53 mmol/g at 70 °C, with an exceptional regression correlation coefficient exceeding 0.9999.

The utilization of biomass-derived MC templated by dual salts presents a promising avenue for constructing core-membrane microstructure via PEI for CO_2 capture, leveraging well-defined mesopore structures and microenvironments. Through impregnation with PEI, particularly PEI with smaller average molecular weights, substantial enhancements in CO_2 sorption performance are achievable. These findings underscore the potential of core-membrane microstructured dual-salt templated MC as efficient sorbents for CO_2 capture applications. Further research and development in this realm hold promise for advancing the field of carbon capture and addressing environmental challenges associated with greenhouse gas emissions.

Acknowledgements This work was supported by the National Natural Science Foundation of China (Grant Nos. 523B2057 and 52236004) and the Non-carbon energy conversion and utilization institute under the Shanghai Class IV Peak Disciplinary Development Program.

Competing Interests The authors declare that they have no competing interest.

Electronic Supplementary Material Supplementary material is available in the online version of this article at https://doi.org/10.1007/s11708-024-0964-2 and is accessible for authorized users.

References

1. Gür T M. Carbon dioxide emissions, capture, storage and utilization: Review of materials, processes and technologies. Progress in Energy and Combustion Science, 2022, 89: 100965
2. Wang Z, Li Z, Liu L, et al. Green synthesis of polypyrrole for CO_2 capture from humid flue gases. Green Chemistry, 2023, 25(4): 1513–1521
3. Zhang C, Zhang D, Zhang X, et al. Rubik's cube-shaped Linde type A zeolite synthesized from biomass for carbon dioxide capture. Cell Reports. Physical Science, 2024, 5(4): 101889
4. Ma Q, Wang S, Fu Y, et al. China's policy framework for carbon capture, utilization and storage: Review, analysis, and outlook. Frontiers in Energy, 2023, 17(3): 400–411
5. Xie J, Li K, Fan J, et al. Lifecycle carbon footprint and cost assessment for coal-to-liquid coupled with carbon capture, storage, and utilization technology in China. Frontiers in Energy, 2023, 17(3): 412–427
6. Seok Chae Y, Park S, Won Kang D, et al. Moisture-tolerant diamine-appended metal–organic framework composites for effective indoor CO2 capture through facile spray coating. Chemical Engineering Journal, 2022, 433: 133856
7. Lyu H, Chen O I F, Hanikel N, et al. Carbon dioxide capture chemistry of amino acid functionalized metal-organic frameworks in humid flue gas. Journal of the American Chemical Society, 2022, 144(5): 2387–2396
8. Al-Absi A A, Mohamedali M, Domin A, et al. Development of in situ polymerized amines into mesoporous silica for direct air CO_2 capture. Chemical Engineering Journal, 2022, 447: 137465
9. Chen H, Dong S, Zhang Y, et al. A comparative study on energy efficient CO_2 capture using amine grafted solid sorbent: Materials characterization, isotherms, kinetics and thermodynamics. Energy, 2022, 239: 122348
10. Zhang C, Zhang Y, Su T, et al. Molecular simulation on carbon dioxide capture performance for carbons doped with various elements. Energy Storage and Saving, 2023, 2(2): 435–441
11. Shi L, Hu T, Xie R, et al. Dual synergistic effect of the amine-functionalized MIL-101@cellulose sorbents for enhanced CO_2 capture at ambient temperature. Chemical Engineering Journal, 2024, 481: 148566
12. Kumar D R, Rosu C, Sujan A R, et al. Alkyl-aryl amine-rich molecules for CO_2 removal via direct air capture. ACS Sustainable Chemistry & Engineering, 2020, 8(29): 10971–10982
13. Gaikwad S, Kim Y, Gaikwad R, et al. Enhanced CO_2 capture capacity of amine-functionalized MOF-177 metal organic framework. Journal of Environmental Chemical Engineering, 2021, 9(4): 105523
14. Zhang C, Su T, Zhang X, et al. Porous core-membrane microstructured nanomaterial composed of deep eutectic solvents and MOF-808 for CO_2 capture. ChemSusChem, 2023, 16(24): e202300864
15. He Z J, Wang Y Z, Miao Y H, et al. Mixed polyamines promotes CO_2 adsorption from air. Journal of Environmental Chemical Engineering, 2022, 10(2): 107239
16. Zhang J, Zuo J, Ai W, et al. Preparation of mesoporous coal-gasification fine slag adsorbent via amine modification and applications in CO_2 capture. Applied Surface Science, 2021, 537: 147938
17. Miao Y, He Z, Zhu X, et al. Operating temperatures affect direct air capture of CO_2 in polyamine-loaded mesoporous silica. Chemical Engineering Journal, 2021, 426: 131875
18. Min Y J, Ganesan A, Realff M J, et al. Direct air capture of CO_2 using poly(ethyleneimine)-functionalized expanded poly(tetrafluoroethylene)/silica composite structured sorbents. ACS Applied Materials & Interfaces, 2022, 14(36): 40992–41002
19. Zhang S, Pan Q, Wang Y. Sunlight-controlled CO_2 separation resulting from a biomass-based CO_2 absorber. Green Energy & Environment, 2022, 7(3): 566–574
20. Zhu X C, Ge T S, Yang F, et al. Efficient CO_2 capture from ambient air with amine-functionalized Mg–Al mixed metal oxides. Journal of Materials Chemistry. A, Materials for Energy and Sustainability, 2020, 8(32): 16421–16428
21. Kumar R, Bandyopadhyay M, Pandey M, et al. Amine-impregnated nanoarchitectonics of mesoporous silica for capturing dry and humid 400 ppm carbon dioxide: A comparative study. Microporous and Mesoporous Materials, 2022, 338: 111956
22. Nezam I, Xie J W, Golub K W, et al. Chemical kinetics of the autoxidation of poly(ethylenimine) in CO_2 sorbents. ACS Sustainable Chemistry & Engineering, 2021, 9(25): 8477–8486
23. Chen Q, Wang S, Rout K R, et al. Development of polyethylenimine (PEI)-impregnated mesoporous carbon spheres for low-concentration CO_2 capture. Catalysis Today, 2021, 369: 69–76
24. Liu Y, Xiao M, Liu S, et al. A novel oil-water microemulsion strategy for controllable synthesis of large mesoporous carbon nanoparticles. Carbon, 2022, 200: 361–374
25. Qiu Y, Zhang C, Zhang R, et al. Integration of pore structure modulation and B, N co-doping for enhanced capacitance deionization of biomass-derived carbon. Green Energy & Environment, 2023, 8(5): 1488–1500
26. Fu J, Shen F, Liu X, et al. Synthesis of MgO-doped ordered mesoporous carbons by Mg^{2+}-tannin coordination for efficient isomerization of glucose to fructose. Green Energy & Environment, 2023, 8(3): 842–851
27. Zhou Q, Di G, Song T, et al. Template synthesis of sulfur-doped mesoporous carbon for efficiently removing gas-phase elemental mercury from flue gas. Fuel, 2022, 321: 124112
28. Luo M, Wang L, Li H, et al. Hierarchical porous biochar from kelp: Insight into self-template effect and highly efficient removal of methylene blue from water. Bioresource Technology, 2023, 372: 128676

29. Park Y M, Kim B G, Gao X, et al. Ordered mesoporous Co_3O_4-Al_2O_3 bimetal oxides for CO_2 hydrogenation to synthetic natural gas: Effects of surface Al_2O_3 distribution. Fuel, 2023, 343: 127943
30. Sani S, Liu X, Li M, et al. Synthesis and characterization of three-dimensional interconnected large-pore mesoporous cellular lignin carbon materials and their potential for CO_2 capture. Microporous and Mesoporous Materials, 2023, 347: 112334
31. Du H, Ren J, Zhang W, et al. Ni nanoparticles *in situ* embedment in 3D ordered macro-/mesoporous carbon framework as efficient microwave absorption and infrared stealth materials. Carbon, 2023, 204: 325–335
32. Wang S, Eberhardt T L, Guo D, et al. Efficient conversion of glucose into 5-HMF catalyzed by lignin-derived mesoporous carbon solid acid in a biphasic system. Renewable Energy, 2022, 190: 1–10
33. Xu C Y, Du R, Yu C B, et al. Glucose-derived micro–mesoporous carbon spheres for high-performance lithium–sulfur batteries. Energy & Fuels, 2023, 37(2): 1318–1326
34. Wu C, Liu J, Wu W, et al. Mild modification of sponge-like carbon: Ammonia post-treatment for enhanced CO_2 adsorption and suitability for supercapacitors. Separation and Purification Technology, 2025, 353: 128525
35. Wu C, Liu J, Wang Y, et al. KCl-assisted activation of macadamia nut shell-derived carbon: Unveiling enhanced pore structure, adsorption and supercapacitor performance. Separation and Purification Technology, 2024, 329: 125188
36. Liu W, Yang J, Liu S, et al. Zinc chloride-activated micro-mesoporous carbon material derived from energy grass and its electrocatalytic performance toward oxygen reduction reaction. Journal of Energy Storage, 2022, 46: 103697
37. Ma Z, Zhang H, Yang Z, et al. Highly mesoporous carbons derived from biomass feedstocks templated with eutectic salt $ZnCl_2$/KCl. Journal of Materials Chemistry. A, Materials for Energy and Sustainability, 2014, 2(45): 19324–19329
38. Zhang C, Zhang X, Su T, et al. Modification schemes of efficient sorbents for trace CO_2 capture. Renewable & Sustainable Energy Reviews, 2023, 184: 113473
39. Xu Z, Zhang X, Yang X, et al. Synthesis of Fe/N co-doped porous carbon spheres derived from corncob for supercapacitors with high performances. Energy & Fuels, 2021, 35(17): 14157–14168
40. Li Z, Deng L, Kinloch I A, et al. Raman spectroscopy of carbon materials and their composites: Graphene, nanotubes and fibres. Progress in Materials Science, 2023, 135: 101089
41. Yu J, Guo M, Muhammad F, et al. One-pot synthesis of highly ordered nitrogen-containing mesoporous carbon with resorcinol–urea–formaldehyde resin for CO_2 capture. Carbon, 2014, 69: 502–514
42. Wang J, Chen H, Zhou H, et al. Carbon dioxide capture using polyethylenimine-loaded mesoporous carbons. Journal of Environmental Sciences, 2013, 25(1): 124–132
43. Choi S, Gray M L, Jones C W. Amine-tethered solid adsorbents coupling high adsorption capacity and regenerability for CO_2 capture from ambient air. ChemSusChem, 2011, 4(5): 628–635
44. Zhang H, Liu R, Xin Y, et al. Enhancing lignin model compound depolymerization using mediator-enzyme catalysis: A sustainable approach to C–C bond cleavage. ACS Sustainable Chemistry & Engineering, 2024, 12(15): 5842–5849
45. Chen M, Yan Z, Luan J, et al. π-π electron-donor-acceptor (EDA) interaction enhancing adsorption of tetracycline on 3D PPY/CMC aerogels. Chemical Engineering Journal, 2023, 454: 140300
46. Walleni C, Malik S B, Missaoui G, et al. Selective NO_2 gas sensors employing nitrogen- and boron-doped and Co-doped reduced graphene oxide. ACS Omega, 2024, 9(11): 13028–13040
47. Cui Q, Zhang M, Chen M, et al. Comparative studies of sulfadiazine sodium degradation performance and mechanisms in the systems of persulfate with and without activation. Chemical Engineering Journal, 2024, 483: 149356
48. Wan S, Fang S, Jiang L, et al. Strong, conductive, foldable graphene sheets by sequential ionic and π bridging. Advanced Materials, 2018, 30(36): 1802733
49. Xu J, Lin W, Long J, et al. Efficient photocatalytic cleavage of C–C bonds in β-1 lignin models and aromatic vicinal diols by combining alkali metal-treated graphitic carbon nitride and persulfate. ACS Sustainable Chemistry & Engineering, 2024, 12(3): 1343–1352
50. Wang S, Kong R. Analyzing the flotation kinetics of long-flame coal slurry using water-soluble emulsified collector mixtures. Fuel, 2024, 360: 130572
51. Xia X, Liao Z, Deng J, et al. Efficient purification of low-level uranium-containing wastewater by polyamine/amidoxime synergistically reinforced fiber. Environmental Pollution, 2024, 344: 123269
52. Torrisi L, Silipigni L, Cutroneo M, et al. Graphene oxide as a radiation sensitive material for XPS dosimetry. Vacuum, 2020, 173: 109175
53. Dods M N, Weston S C, Long J R. Prospects for simultaneously capturing carbon dioxide and harvesting water from air. Advanced Materials, 2022, 34(38): 2204277
54. Sani S, Liu X, Stevens L, et al. Amine functionalized lignin-based mesoporous cellular carbons for CO_2 capture. Fuel, 2023, 351: 128886
55. Gibson J A A, Gromov A V, Brandani S, et al. The effect of pore structure on the CO_2 adsorption efficiency of polyamine impregnated porous carbons. Microporous and Mesoporous Materials, 2015, 208: 129–139
56. Tang Z, Han Z, Yang G, et al. Polyethylenimine loaded nanoporous carbon with ultra-large pore volume for CO_2 capture. Applied Surface Science, 2013, 277: 47–52
57. Chai S H, Liu Z M, Huang K, et al. Amine functionalization of microsized and nanosized mesoporous carbons for carbon dioxide capture. Industrial & Engineering Chemistry Research, 2016, 55(27): 7355–7361
58. Yan H, Zhang G, Liu J, et al. Investigation of CO_2 adsorption performance of amine impregnated adsorbents using amine-support matching strategies. Separation and Purification Technology, 2023, 310: 123178
59. Kong W, Liu J. Ordered mesoporous carbon with enhanced porosity to support organic amines: Efficient nanocomposites for the selective capture of CO_2. New Journal of Chemistry, 2019, 43(15): 6040–6047